RSC Advances

PAPER

View Article Online
View Journal | View Issue

Cite this: *RSC Adv.*, 2020, **10**, 8973

A flower-like CoS_2/MoS_2 heteronanosheet array as an active and stable electrocatalyst toward the hydrogen evolution reaction in alkaline media†

Mengtong Shi,[ab] Yang Zhang,[*bc] Yaxing Zhu,[b] Wei Wang,[b] Changzheng Wang,[*a] Aifang Yu,[bc] Xiong Pu[bc] and Junyi Zhai[*bc]

Received 27th December 2019
Accepted 24th February 2020

DOI: 10.1039/c9ra10963c

rsc.li/rsc-advances

CoS_2/MoS_2 heteronanosheet arrays (HNSAs) with vertically aligned flower-like architectures are fabricated through *in situ* topotactic sulfurization of $CoMoO_4$ nanosheet array (NSA) precursors on conductive Ni foam. $CoMoO_4$ NSAs are prepared by a self-template hydrothermal method without using any hard template and surfactant. Benefiting from a 3D flower-like architecture constituted by ultrathin nanosheets with abundant exposed heterointerfaces as highly active sites and predesigned void spaces, the as-synthesized CoS_2/MoS_2 HNSAs exhibit an excellent hydrogen evolution reaction (HER) performance with a low overpotential of 50 mV at 10 mA cm^{-2}, and a small Tafel slope of 76 mV dec^{-1} in 1.0 M KOH, which outperforms most previously reported CoS_2 and MoS_2 based electrocatalysts with compositional or morphological similarity. This work demonstrates the great potential in developing high-efficiency and earth-abundant electrocatalysts for alkaline HER through heterointerface engineering and morphological design by utilizing transition metal molybdate as a promising platform.

1. Introduction

Water splitting has been widely regarded as a promising approach towards sustainable hydrogen generation from aqueous solution. Development of hydrogen evolution reaction (HER) and oxygen evolution reaction (OER) electrocatalysts with high-efficiency, long-term durability comparable to precious-metal based electrocatalysts is one of the key building blocks for any future renewable energy system.[1] However, electrochemical water splitting suffers severely from sluggish HER kinetics in high concentration alkaline solutions. Considering the high price and scarcity of Pt, a variety of transition metal based compounds and composites have been recently investigated for alkaline HER, including metal alloys,[2,3] sulfides,[4,5] carbides,[6,7] nitrides[8,9] and phosphides[10,11] due to their abundance, high reactivity, electrochemical stability. In particular, transition metal sulfides are among the most investigated noble-metal-free candidates and have recently attracted substantial research interest as low-cost and active alternative electrocatalysts for alkaline HER.[12–14] The previous works revealed that both morphological control and interface engineering played indispensable roles in boosting the electrocatalytic performance of nanostructured transition metal dichalcogenide composites. Compared to mono-metal sulfides, such as NiS_2 and CoS_2, bi-metallic or mixed-metal sulfides (*e.g.*, $Ni_{0.33}Co_{0.67}S_2$ and $NiCo_2S_4$) demonstrated a higher HER electrocatalytic activity mainly due to the exposure of electrochemically active surface edge sites.[15,16] Moreover, chemical doping and incorporation approaches played an essential role in boosting electrocatalytic performance through the modulation of intrinsic activity and electronic structures, such as N-doped Ni_3S_2 nanosheet arrays, Co-doped mesoporous MoS_2 foam and O-incorporated MoS_2 nanosheets.[17–20] Transition metal dichalcogenide based nanocomposites were investigated as well, demonstrating enhanced electrocatalytic performance due to the heterointerfaces acting as accessible and stable active sites. For instance, various electrocatalysts with core/shell nanostructures have been recently investigated, such as CoS_2/MoS_2 nanowires, Ni_3S_2/MoS_2 nanorods, Ni_3S_2/MoS_2 nanoparticles and MoC/Mo_2C nanowires, *etc.*[6,21–23] Those synergistically enhanced electrocatalytic performances of transition metal dichalcogenides or carbides could pave a pathway for achieving sustainable energy conversion.

The development of environmentally-friendly and facile synthetic routes for electrocatalysts with tunable morphology and composition to maximize the number of active surface sites still remains a challenging task. The fabrication of active electrocatalysts on a conductive substrate, such as Ni foam/foil,

[a]*Key Laboratory of Urban Stormwater System and Water Environment, Ministry of Education, Beijing University of Civil Engineering and Architecture, Beijing 100044, China. E-mail: changzhwang@163.com*

[b]*Beijing Institute of Nanoenergy and Nanosystems, Chinese Academy of Sciences, Beijing 100083, China. E-mail: zhangyang@binn.cas.cn; jyzhai@binn.cas.cn*

[c]*School of Nanoscience and Technology, University of Chinese Academy of Sciences, Beijing 100049, China*

† Electronic supplementary information (ESI) available: EDS spectra of $CoMoO_4$ NSAs and CoS_2/MoS_2 HNSAs, and cyclic voltammograms of 3D flower-like CoS_2/MoS_2 HNSAs. See DOI: 10.1039/c9ra10963c

carbon fiber/cloth or Ti foil, could provide the efficient pathways for charge transport and open channels for rapid release of H_2 bubbles during HER process.[24] Among different approaches for synthesizing transition metal sulfides electrocatalysts, synergistic effects of morphological control and heterointerface engineering strongly significantly depend on the appropriate choice of precursors. Transition metal oxides and hydroxides with various nanostructures have been employed as precursors to synthesize transition metal sulfide based composites.[21,25,26] A transformation process of transition metal oxides or hydroxides to transition metal sulfides would occur in a sulfur vapor atmosphere or ions solutions. According to previous works, metal molybdate ($AMoO_4$) comprising molybdenum and second transition metals (A = Fe, Co and Ni, *etc.*) could be prepared by several convenient synthetic approaches.[27] Although diverse metal molybdates have been reported to exhibit excellent performance in supercapacitor devices, those metal molybdates were found to be nearly inactive towards the HER.[4,28–33] Recent studies shed light on the role of metal molybdates as potential precursors towards the rational design of transition metal dichalcogenides heterointerface through the simultaneous sulfurization of corresponding molybdenum and second transition metal. For instance, Yu *et al.* reported that $NiMoO_4$ nanowires were employed as the precursor for the preparation of bi-metal sulfide NiS_2/MoS_2 heteronanowires, which exhibiting an improved HER performance in comparison with NiS_2 and MoS_2.[4] In order to further improve the electrocatalytic performance, great endeavors have been made to overcome the bottlenecks associated with the use of insulating binders and inactive conductive agent due to the serious concerns on the reduced number of exposed active edge sites and the increased resistance between the electrocatalyst and electrode.[24] It should be highlighted that some of metal molybdates can be directly grown on the conducting substrates through a facile one-step hydrothermal approach.[32,34] Recently, Zheng *et al.* recently reported the synthesis of $NiMoO_4$ nanowire array on the Ti foil and the conversion to NiS_2/MoS_2 heteronanowire array with enhanced HER performance.[35] Due to their inherent characteristics, numerous molybdate compounds could be considered as prospective precursors for the synthesis of transition metal dichalcogenides, aiming at taking the advantages of synergistic effect through the optimization of precursor morphology and heterointerface engineering. In fact, the development of 3D integrated electrodes fabricated by electroactive nanomaterials are appealing not only in electrochemical water splitting but other electrochemical energy conversion and storage systems as well.

Herein, we developed a facile strategy to synthesize 3D flower-like CoS_2/MoS_2 heteronanosheet arrays (HNSAs) on conductive Ni foam by *in situ* topotactic conversion of $CoMoO_4$ nanosheet arrays (NSAs) precursor. The simultaneous sulfurization of Co and Mo in $CoMoO_4$ precursor led to the formation of CoS_2/MoS_2 nanocomposite while the structural and morphological characteristic of ultrathin nanosheets was well retained during the vapor phase sulfurization process. The as-prepared CoS_2/MoS_2 HNSAs demonstrated an excellent HER activity with a low overpotential of 50 mV at current density of 10 mA cm^{-2} and a small Tafel slope of 76 mV dec^{-1} in 1.0 KOH. The superior HER performance of CoS_2/MoS_2 HNSAs could be attributed to the following three aspects: (i) the abundant accessible CoS_2/MoS_2 heterointerface served as highly active catalytic sites after *in situ* topotactic sulfurization; (ii) 3D flower-like CoS_2/MoS_2 HNSAs integrating directly on the conductive Ni foam facilitated fast electron transport; (iii) the 3D network structure of CoS_2/MoS_2 HNSAs offered the internal void spaces between neighboring heteronanosheets, which were suitable for both the diffusion of electrolyte and release of gas bubble process. This work serves as a proof of concept for the heterointerface engineering of transition metal dichalcogenides nanocomposite as efficient electrocatalysts through rational compositional and morphological control.

2. Experimental section

2.1 Chemicals

All of the chemicals were purchased from Alfa Aesar and used as received without further purification, including sublimed S powder, $Na_2MoO_4 \cdot 2H_2O$ and $Co(NO_3)_2 \cdot 6H_2O$. The porous Ni foams were obtained from Kunshan Company.

2.2 Materials synthesis

The Ni foams (1.0 cm × 1.5 cm) were cleaned in acetone, absolute ethanol, HCl solution for 30 min, respectively. The preparation of 3D flower-like $CoMoO_4$ NSAs was conducted as follow, 1.6 mM $Na_2MoO_4 \cdot 2H_2O$ and 1.6 mM $Co(NO_3)_2 \cdot 6H_2O$ was dissolved under continuous stirring in 20 mL deionized water. The pretreated Ni foams were then immersed into the mixed solution and kept at 90 °C in an electrical oven for 48 h. After cooling to the room temperature, the as-prepared $CoMoO_4$ NSAs on Ni foam were washed with the assistance of sonication to remove surface residues and then dried at 60 °C in a vacuum oven for overnight. The *in situ* topotactic sulfurization was conducted by a vapor phase sulfurization procedure. $CoMoO_4$ NSAs precursor was converted to CoS_2/MoS_2 HNSAs at 370 °C for 45 min. Mass loading of CoS_2/MoS_2 HNSAs on Ni foam was 0.9 mg cm^{-2}.

2.3 Materials characterization

The morphology of the as-prepared 3D flower-like $CoMoO_4$ NSAs and CoS_2/MoS_2 HNSAs were characterized by field emission scanning electron microscopy (SEM, SU8020, Hitachi), transmission electron microscopy (TEM, F20 and Talos F200S, FEI) with an energy-dispersive X-ray spectroscopy (EDS) detector. The crystal structure of all samples was characterized by X-ray diffraction (XRD, X'Pert^3 Powder diffractometer, Cu Kα radiation (λ = 1.5418 nm)). The chemical composition and valence state of $CoMoO_4$ NSAs and CoS_2/MoS_2 HNSAs was investigated by X-ray photoelectron spectroscopy (XPS, ThermoFisher Scientific ESCALAB 250Xi).

2.4 Electrochemical characterization

The electrochemical measurements of 3D flower-like CoS_2/MoS_2 HNSAs were conducted in a three-electrode system using a CHI

660E electrochemical workstation (CH Instruments, Shanghai, China). The 3D flower-like CoS_2/MoS_2 HNSAs were used as working electrode with a fixed geometric area of 1 cm × 1 cm, while Hg|HgO and graphite rod was used as the reference electrode and counter electrode, respectively. In this work, the HER activity of 3D flower-like CoS_2/MoS_2 HNSAs was performed in 1.0 M KOH solution while all applied potentials were converted with respect to reversible hydrogen electrode (RHE). Linear sweep voltammetry (LSV) with a scan rate of 5 mV s^{-1} was conducted without *iR* compensation. The electrochemical double-layer capacitance (C_{dl}) was measured basing on the data of cyclic voltammetry (CV) at various scan rates (10, 20, 30, 40, 50 and 60 mV s^{-1}) in range between 0.1 and 0.2 V (*versus* RHE). The long-term stability was conducted by chronoamperometry and 2000 cycles continuously in 1.0 M KOH, respectively. Electrochemical impedance spectroscopy (EIS) measurements were carried out at an overpotential of 150 mV in a frequency range from 100 kHz to 0.01 Hz. The KOH solution was purged with high-purity N_2 to remove dissolved oxygen before each electrochemical measurement.

3. Results and discussion

Inspired by recent studies of *in situ* synthesis of transition metal dichalcogenides based electrocatalysts on conductive substrate, the high density and uniformly distributed nanoarray architectures, such as 1D nanowire/rod and 2D nanosheet arrays, can significantly improve the HER catalytic activity and stability. The fabrication of 3D flower-like CoS_2/MoS_2 HNAS on conductive Ni foam were facilely conducted by a two-step procedure without using any surfactant and hard template. The synthetic process and composition evolution of CoS_2/MoS_2 HNSAs is schematically illustrated in Fig. 1.

The flower-like $CoMoO_4$ NSAs were synthesized on porous Ni foam *via* a self-template method (see Experimental section for more details).[36,37] As shown in Fig. 2a and b, the low-magnification scanning electron microscopy (SEM) images demonstrate that the 3D network structure of flower-like $CoMoO_4$ NSAs anchored on Ni foam. The self-assembled $CoMoO_4$ nanosheets with lateral sizes of about 2 μm were grown uniformly on Ni foam surface with a 3D flower-like micro/nanostructure (Fig. 2c). It can be explained by the large amount of nanosized $CoMoO_4$ nucleation clusters were formed in the solution for the self-assembly of 2D nanosheets, which further led to the formation of flower-like morphology. The high-magnification SEM image exhibits the as-synthesized $CoMoO_4$ nanosheets with thickness in the range of 10–20 nm are interconnected with each other (Fig. 2d), providing a large number of internal void spaces between adjacent nanosheets. It can be also observed some $CoMoO_4$ nanosheets with slightly curved surface and crumpled edges due to the larger lateral dimension than the thickness. Transmission electron microscopy (TEM) characterizations were conducted to investigate the structure of $CoMoO_4$ nanosheets. Fig. 2e and f presents that 3D flower-like $CoMoO_4$ micro/nanostructure is made up of interconnected nanosheets with a lateral size of several hundred nanometers. It is found that the $CoMoO_4$ nanosheets are slightly folded in some regions. For instance, the observation of dark strips resulted from the curled edges or wrinkles of the $CoMoO_4$ nanosheets which is consistent with the SEM observation. Fig. 2g shows the enlarged TEM image of $CoMoO_4$ nanosheet edge, revealing the existence of slight disorder. From high resolution TEM (HRTEM) image, the lattice spacing is 0.33 nm corresponding well to (002) plane of monoclinic $CoMoO_4$ (Fig. 2i).[34,38] The high-angle annular dark-field scanning TEM (HAADF-STEM) and corresponding energy-dispersive X-ray spectroscopy (EDS) characterization (Fig. 2i–l) confirms the uniform distributions of Co, Mo and O elements throughout the 3D flower-like nanosheets. XRD pattern shows no obvious characteristic peak of the $CoMoO_4$ NSAs, indicating the polycrystalline nature of self-assembled nanosheets through the low temperature hydrothermal method.[32]

Owing to the morphological features of ultrathin $CoMoO_4$ nanosheets, the *in situ* topotactic conversion to CoS_2/MoS_2

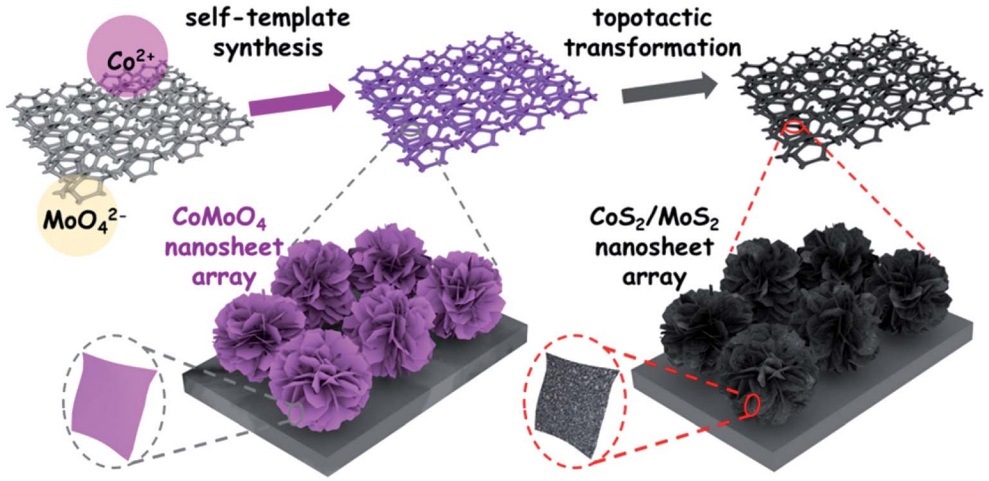

Fig. 1 Schematic illustration for the self-template synthesis of 3D flower-like $CoMoO_4$ NSAs and *in situ* topotactic sulfurization to CoS_2/MoS_2 HNSAs.

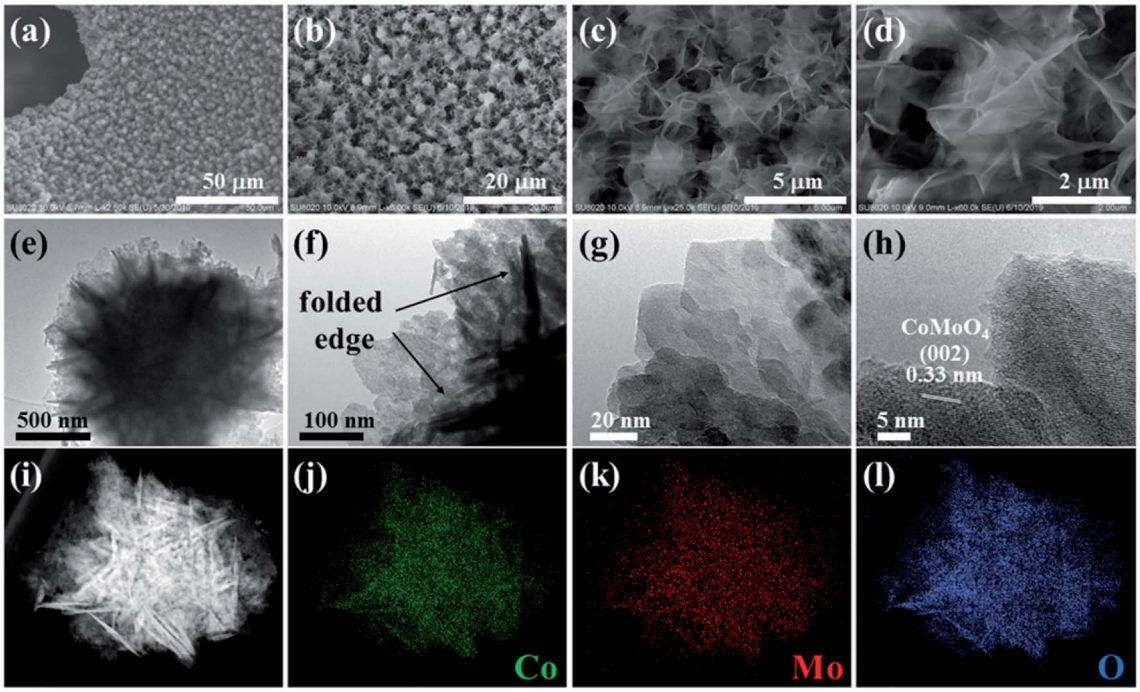

Fig. 2 (a–d) SEM images, (e–h) TEM images, (i) HAADF-STEM and (j–l) EDS mapping images of 3D flower-like $CoMoO_4$ nanosheets.

nanosheets was successfully achieved by the vapor phase sulfurization process. Fig. 3a–d demonstrates the dense and uniform coverage of flower-like CoS_2/MoS_2 HNSAs. Compared to $CoMoO_4$ nanosheets with a relative smooth surface, the high-magnification SEM image undoubtedly reveals that the coarse surface of CoS_2/MoS_2 heteronanosheets after sulfurization (Fig. 3d). Basing on the morphology evolution, it can be seen that the flower-like $CoMoO_4$ NSAs acted as a self-template for the topotactic conversion to CoS_2/MoS_2 HNSAs. Similar to the case of $CoMoO_4$ nanosheets, CoS_2/MoS_2 heteronanosheets with transparent feature indicated the ultrathin nature was also retained after the *in situ* conversion (Fig. 3e and f). As shown in

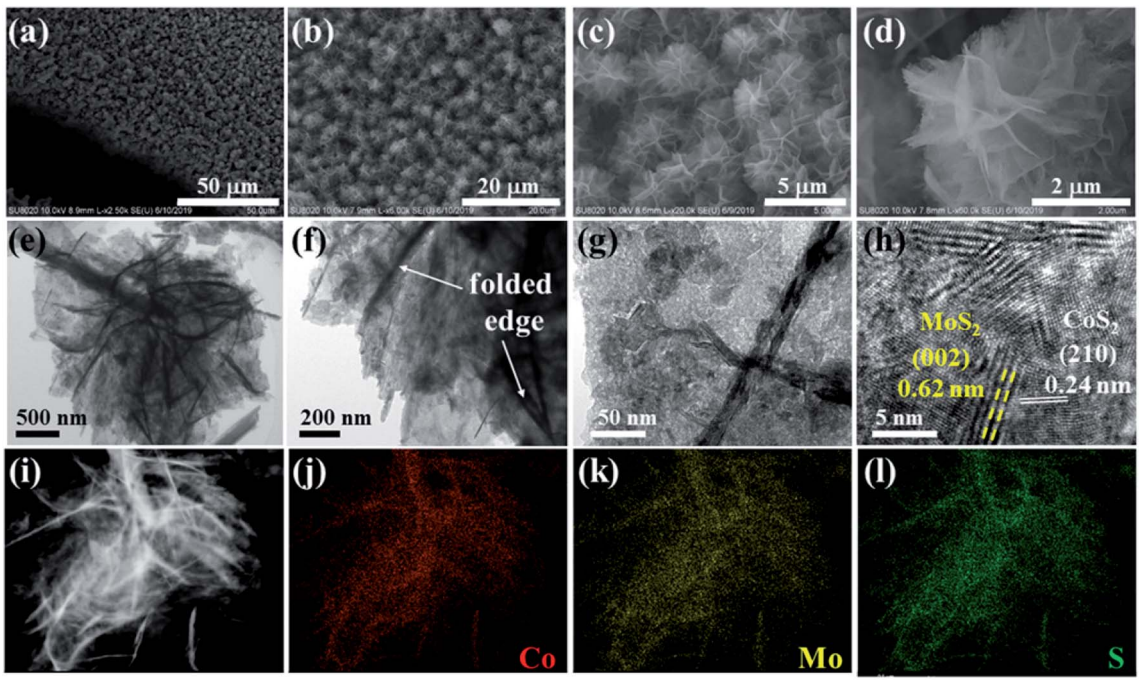

Fig. 3 (a–d) SEM images, (e–h) TEM images, (i) HAADF-STEM and (j–l) EDS mapping images of 3D flower-like CoS_2/MoS_2 nanosheets.

Fig. 3g, the enlarged TEM image demonstrates that heteronanosheet integrated with CoS_2 and MoS_2 species after sulfurization. The HRTEM image reveals lattice fringes of 0.62 and 0.24 nm, corresponding to the (002) plane of MoS_2 and (210) plane of CoS_2, respectively (Fig. 3h). The observation of lattice discontinuities in CoS_2/MoS_2 heteronanosheet indicates the existence of the slight disordered structure. On the one hand, a large number of heterointerface forming between CoS_2 and MoS_2 can be undoubtedly identified. On the other hand, the intimate contact of CoS_2 and MoS_2 can be ascribed to the simultaneous sulfurization of Co and Mo in $CoMoO_4$ precursor. It should be noted that the as-obtained heteronanosheets demonstrated a relatively uniform distribution of CoS_2 and MoS_2 species. Furthermore, the elemental distributions of 3D flower-like CoS_2/MoS_2 nanosheets were characterized by HAADF-STEM and the corresponding EDS characterizations, revealing the homogeneous distribution of Co, Mo and S throughout the whole heteronanosheets (Fig. 3i–l). As shown in Fig. S1 (ESI†), the EDS spectra analysis further confirmed $CoMoO_4$ NSAs were transformed to CoS_2/MoS_2 HNSAs after *in situ* topotactic sulfurization due to the disappearance of O signal and appearance of S signal. The overlapping Co, Mo and S signals indicates the uniform formation of CoS_2 and MoS_2 nanocomposites while the predesigned void spaces can still be observed between neighboring heteronanosheets. Attributed to the good preservation of 3D network structure of $CoMoO_4$ precursor after *in situ* topotactic conversion, 3D flower-like CoS_2/MoS_2 HNSAs exhibit porous structures which is essential to increase the accessible surface areas and facilitate the effective contact between electrocatalyst and electrolyte ions.

To confirm the composition and valence states of the as-prepared flower-like $CoMoO_4$ NSAs and CoS_2/MoS_2 HNSAs, X-ray photoelectron spectroscopy (XPS) characterization were conducted. For the $CoMoO_4$ NSAs, the Co 2p spectrum exhibits two main peaks at 780.8 and 797.1 eV (Fig. 4a), corresponding to the low energy band of Co $2p_{3/2}$ and high energy band of Co $2p_{1/2}$, respectively, as well as their satellite peaks (denoted as "sat.").[39] In the Mo 3d spectrum of $CoMoO_4$ precursor, two significant peaks at 232.1 and 235.3 eV are associated with Mo $3d_{5/2}$ and Mo $3d_{3/2}$ electronic configurations, respectively, indicating a +6 oxidation state of Mo in the $CoMoO_4$ NSAs (Fig. 4b). As shown in Fig. 4c, the O 1s spectrum of $CoMoO_4$ precursor can be deconvoluted into four peaks at 530.2, 530.9, 531.8 and 533.0 eV, corresponding to the Co–O bonds, hydroxyl groups in the hydrated sample, oxygen ions in low coordination and physic- and/or chemisorbed water, respectively.[40] After sulfurization, the XPS spectrum of Co $2p_{3/2}$ and Co $2p_{1/2}$ signals are found to be 778.9 and 793.9 eV, respectively. The obvious shifts of Co $2p_{3/2}$ and Co $2p_{1/2}$ binding energy indicate the formation of CoS_2 after *in situ* sulfurization because sulfur has a lower electronegativity than oxygen (see Fig. 4d). As shown in Fig. 4e, two characteristic peaks at the binding energies of 228.8 and 232.0 eV are ascribed to Mo $3d_{5/2}$ and Mo $3d_{3/2}$, indicating a +4 oxidation state of Mo and therefore confirming the conversion of MoS_2 after *in situ* topotactic sulfurization.[21] It should be noted the observation of broad S 2s peaks around 226.0 eV suggests the formation of Co–S and Mo–S bonding. The analysis of the S 2p spectrum reveals the characteristic peaks at 161.6 and 162.6 eV are assigned to S $2p_{3/2}$ due to the formation of Co–S and Mo–S bonding while the broad peak around 163.2 and 164.2 eV is attributed to bridging S_2^{2-} between CoS_2 and MoS_2 (Fig. 4f), which were identified as active HER sites.[41–43] Therefore, it can be concluded that the formation of CoS_2/MoS_2 nanocomposite *via in situ* topotactic conversion.

To evaluate the electrocatalytic activity for HER, 3D flower-like CoS_2/MoS_2 HNSAs was tested in a 1.0 M KOH solution using a typical three-electrode configuration. Fig. 5a demonstrates the polarization curves without *iR* correction. The overpotential for 3D flower-like CoS_2/MoS_2 HNSAs to achieve a current density of 10 mA cm^{-2} (η_{10}) is 50 mV (*vs.* RHE) while the conductive Ni foam demonstrated negligible HER activity. In comparison with the previously reported transition metal sulfides based electrocatalysts (Table S1 in ESI†), the η_{10} of 3D

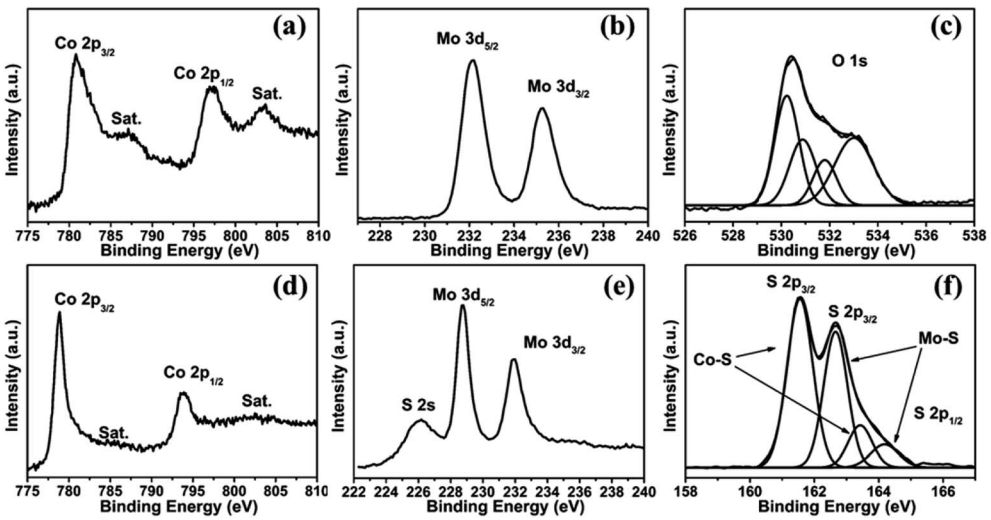

Fig. 4 High-resolution XPS profiles of (a) Co 2p, (b) Mo 3d and (c) O 1s in $CoMoO_4$ NSAs; (d) Co 2p, (e) Mo 3d and S 2s, and (f) S 2p in CoS_2/MoS_2 HNSAs.

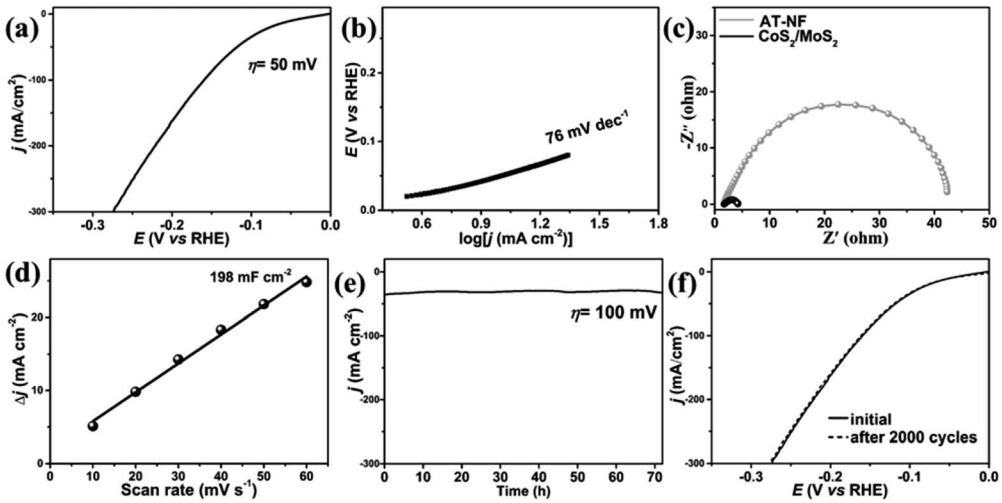

Fig. 5 (a) Polarization curves and (b) Tafel plots of as-synthesized 3D flower-like CoS_2/MoS_2 HNSAs, (c) Nyquist plots of acid-treated Ni foam and 3D flower-like CoS_2/MoS_2 HNSAs in 1.0 M KOH at $\eta = 150$ mV, (d) the differences in the current density (Δj) at 0.15 V *vs.* RHE plotted against scan rate fitted to a linear region for the calculation of C_{dl}, (e) the long-term durability test of CoS_2/MoS_2 HNSAs at $\eta = 100$ mV, (f) stability for CoS_2/MoS_2 NSAs with initial polarization curve and after 2000 cycles.

flower-like CoS_2/MoS_2 HNSAs is much lower those of the reported $NiCo_2S_4$ nanowire arrays (210 mV),[15] $Ni_{0.33}Co_{0.67}S_2$ nanowire arrays (88 mV),[16] Ni–Mo–S nanowire networks (210 mV),[44] MoS_2 nanosheet arrays (200 mV),[45] Ni_3S_2 nanosheet arrays (223 mV),[46] CoS_2 nanosheet arrays (192 mV),[47] FeS_2 mesoporous nanoparticles (96 mV),[48] Ni_3S_2 nanorod arrays (200 mV),[49] Na-doped 1T-MoS_2 nanosheets (183 mV)[50] and 1T-$MoSe_2$ nanosheets (152 mV).[51] In particular, the electrocatalytic performance of 3D flower-like CoS_2/MoS_2 HNSAs is also comparable to the noble metal doped or decorated transition metal sulfides, such as Pt–MoS_2 nanosheet clusters (60 mV),[52] Pt–MoS_2 nanoparticles (58 mV)[53] and Rh–MoS_2 nanosheets (47 mV).[54] *Via* further comparison with other Co-, Mo- and Ni-based heterostructured electrocatalysts (Table S1, ESI†), the electroactivity of 3D flower-like CoS_2/MoS_2 HNSAs is better than those of CoS_2/MoS_2 nanosheet composites (154 mV),[55] MoS_2/CoS_2 nanowire arrays (87 mV),[21] NiS_2/CoS_2/C carnation-like nanosheets (165 mV),[56] Co_9S_8/MoS_2 core/shell nanocrystals (97 mV),[57] MoS_2/NiS/MoO_3 nanowire arrays (90 mV),[58] NiS_2/MoS_2 nanowires (204 mV),[4] MoS_2/Ni_3S_2 nanorod arrays (98 mV),[22] CoS_2@-MoS_2/RGO composites (98 mV),[59] MoS_2/Ni_3S_2 nanosheets/particles (110 mV),[23] oxygenated-CoS_2/MoS_2 nanosheet arrays (97 mV),[60] CoS_2/MoS_2 nanowire arrays (97 mV)[61] CoS_2–C@MoS_2 nanofibers (173 mV)[62] and Ag_2S/MoS_2/RGO composites (190 mV).[63] In particular, previous report demonstrated CoS_2/MoS_2 nanosheet composites were synthesized through a one-step hydrothermal method.[55] However, the CoS_2/MoS_2 HNSAs demonstrated a remarkable alkaline HER activity, which can be attributed to the formation of heteronanosheet-based flower-like microarchitecture anchored on the Ni foam. It should be highlighted that the Ni foam with porous and conductive characteristics played essential roles in providing more pathways for charge transport and offering open channels for the release of gas bubbles.

Volmer reaction

$$H_2O + M^* + e^- \rightarrow M\text{–}H^* + OH^- \quad (1)$$

Heyrovsky reaction

$$M\text{–}H^* + H_2O + e^- \rightarrow H_2 + OH^- + M^* \quad (2)$$

Tafel reaction

$$M\text{–}H^* + M\text{–}H^* \rightarrow H_2 + 2M^* \quad (3)$$

According to the previous reports, three principal steps were proposed for hydrogen evolution: (1) Volmer reaction with a Tafel slope of ~120 mV dec^{-1}, (2) Heyrovsky reaction with a Tafel slope of ~40 mV dec^{-1}, and (3) Tafel reaction with a Tafel slope of ~30 mV dec^{-1}. It should be noted that the asterisk indicates the active site for HER while M–H* represents the hydrogen atom bound to the active site on electrocatalyst. In fact, the determination of the specific mechanism cannot be achieved by the direct evaluation of the Tafel slope for most of electrocatalysts. As shown in Fig. 5b, the relatively small slope of 3D flower-like CoS_2/MoS_2 HNSAs (76 mV dec^{-1}) falls within the range of 40–120 mV dec^{-1}, which is comparable to those of abovementioned composites, such as CoS_2/MoS_2 nanosheets (61 mV dec^{-1}),[55] MoS_2/CoS_2 nanowire array (73.4 mV dec^{-1}),[21] and Co_9S_8/MoS_2 core/shell nanocrystals (71 mV dec^{-1}),[57] Co_9S_8@MoS_2 nanoparticles (110 mV dec^{-1}),[43] NiS_2/MoS_2 nanowires (65 mV dec^{-1}),[4] MoS_2/Ni_3S_2 nanorod arrays (61 mV dec^{-1}),[22] MoS_2/Ni_3S_2 nanosheets/particles (88 mV dec^{-1}),[23] oxygenated-CoS_2/MoS_2 nanosheet arrays (83.1 mV dec^{-1}),[60] CoS_2/MoS_2 nanowire arrays (78.7 mV dec^{-1})[61] and CoS_2–C@MoS_2 nanofibers (61 mV dec^{-1}).[62] The small Tafel slope of 3D flower-like CoS_2/MoS_2 HNSAs unveils a fast increase of hydrogen generation rate with increasing applied overpotential. It can concluded that the considerably promoted Volmer step in HER kinetics indicates that the Heyrovsky mechanism is dominant for

alkaline HER on 3D flower-like CoS_2/MoS_2 HNSAs.[64] Furthermore, the electrochemical impedance spectroscopy (EIS) measurements were conducted to investigate the electrochemical behavior during the HER process (Fig. 5c). The Nyquist plot of 3D flower-like CoS_2/MoS_2 HNSAs demonstrates the low charge transfer resistance, indicating the fast electron transfer at the solution electrode interfaces. We further investigate the double-layer capacitance (C_{dl}) of as-fabricated 3D flower-like CoS_2/MoS_2 HNSAs, which is known to be proportional to the electrochemical surface area (Fig. S2, ESI†). Fig. 5d plots the capacitive current densities of CoS_2/MoS_2 HNSAs ($\Delta j = j_a - j_b$, where j_a and j_b denotes current densities in CV at 0.15 V (*vs.* RHE)), the C_{dl} value is estimated to be 198 mF cm^{-2}, which is comparable to the previously reported transition metal based electrocatalysts.[26] The large C_{dl} value indicates the enriched active sites for alkaline HER, resulting from a large number of heterointerfaces between CoS_2 and MoS_2 after *in situ* sulfurization. The long-term stability in high concentration alkaline solutions is an essential issue for transition metal dichalcogenides electrocatalysts to be practically applicable.[65] As presented in Fig. 5e, the stability test was conducted for 70 h, there was no apparent change in the current density at $\eta = 100$ mV. As demonstrated in Fig. 5f, the stability test of 3D flower-like CoS_2/MoS_2 HNSAs was also conducted for 2000 CV cycles, indicating the good durability in alkaline media. In comparison with previously reported alkaline HER electrocatalysts, the considerable enhancement in alkaline HER performance of 3D flower-like CoS_2/MoS_2 HNSAs will be discussed in more details below. Basing on the morphological evolution, flower-like $CoMoO_4$ NSAs were employed as precursor for the topotactic conversion of CoS_2/MoS_2 HNSAs with well retained 3D network structure. After sulfurization, the coarse nanosheets surface indicated the homogeneous distribution of CoS_2 and MoS_2 species through the whole nanosheets as well as abundant heterointerfaces. On the one hand, the high conductivity of porous Ni foam enabled the efficient electron transport to 3D flower-like heteronanosheets. On the other hand, the intimate integration of CoS_2 and MoS_2 play a key role in facilitating the faster charge transport through the whole heteronanosheets and then promoted the hydrogen generation. The formation of 3D flower-like heteronanosheet array morphology significantly increased the electroactive surface areas through the exposed active sites and well-exposed heterointerface not only from the nanosheet edges but also the nanosheet surfaces, which considerably facilitated efficient electron and ion transportation as well as the release of as-produced H_2 gas bubbles during the HER process. According to previous studies, multi-layered MoS_2 have rarely shown superior HER performance without surface modification and/or heterointerface engineering because the highly active sites of multilayer MoS_2 are mainly located on the exposed edges instead of the basal plane.[5] The heterointerface between CoS_2 and MoS_2 facilitated electron transfer between Co and Mo through bridging S_2^{2-} species which simultaneously bonding to Co and Mo atoms, leading to the creation of latent active sites.[43] Theoretical studies also indicated that H* preferably adsorbs on these transition metal-site at the localized heterointerface region due to a lower chemisorption free energy, therefore resulting in the remarkably enhanced HER performance.[4] For these reasons, 2D ultrathin heteronanosheets composed of interconnected CoS_2 and MoS_2 species would be highly advantages. Previous studies unveiled that the well-exposed transition metal related active sites could act as an exceptional H_2O dissociation center while the Mo-related active sites demonstrate superior adsorption capability toward H.[4,13,57,66] The formation of well-exposed CoS_2/MoS_2 heterointerfaces may simultaneously promote the adsorption towards H in alkaline media and strengthen the dissociation of H_2O molecules, which require further theoretical investigation.[67,68]

4. Conclusion

In summary, 3D flower-like CoS_2/MoS_2 heteronanosheets array was fabricated on conductive Ni foam through a self-template hydrothermal synthesis and subsequent *in situ* topotactic sulfurization. The morphological design of $CoMoO_4$ nanosheet array as precursor allow the well-retained 3D network structure with large exposed surface areas after sulfurization. CoS_2/MoS_2 heteronanosheet array as efficient electrocatalyst for alkaline HER with a low overpotential of 50 mV at current density of 10 mA cm^{-2} and small Tafel slope of 76 mV dec^{-1}, which is comparable to those of benchmark transition metal based electrocatalysts. Basing on our experimental characterizations, we demonstrated that the enhanced electrocatalytic performance can be mainly attributed to the synergistic effect of rational morphological design of 3D interconnected network structure and the formation of abundant well-exposed CoS_2/MoS_2 heterointerfaces. Out synthetic strategy can possibly be extended to the preparation of other traditional metal dichalcogenide nanocomposite by the rational design of metal molybdate precursor, including substituting Co with other transition metal (such as Fe, Ni or Cu) or tuning their morphology from 2D heteronanosheet to 1D heteronanowire arrays. Further improvement in electrochemical energy conversion and storage systems basing on low-cost and earth-abundant transition metal dichalcogenides can be expected by utilizing the various molybdate precursors to increase the intrinsic activity of non-precious electrocatalysts *via* morphological control and heterointerface engineering.

Conflicts of interest

There are no conflicts of interest to declare.

Acknowledgements

This work is financially supported by the National Natural Science Foundation of China (NSFC 21603014 and 51872031), and BUCEA Post Graduate Innovation Project (PG2019037).

References

1 W. J. Zhou, J. Jia, J. Lu, L. J. Yang, D. M. Hou, G. Q. Li and S. W. Chen, *Nano Energy*, 2016, **28**, 29–43.

2 Q. Zhang, P. Li, D. Zhou, Z. Chang, Y. Kuang and X. Sun, *Small*, 2017, **13**, 1701648.
3 D. Gao, J. Guo, X. Cui, L. Yang, Y. Yang, H. He, P. Xiao and Y. Zhang, *ACS Appl. Mater. Interfaces*, 2017, **9**, 22420–22431.
4 P. Kuang, T. Tong, K. Fan and J. Yu, *ACS Catal.*, 2017, **7**, 6179–6187.
5 J. Xie, H. Zhang, S. Li, R. Wang, X. Sun, M. Zhou, J. Zhou, X. W. Lou and Y. Xie, *Adv. Mater.*, 2013, **25**, 5807–5813.
6 H. Lin, Z. Shi, S. He, X. Yu, S. Wang, Q. Gao and Y. Tang, *Chem. Sci.*, 2016, **7**, 3399–3405.
7 L. Ma, L. R. L. Ting, V. Molinari, C. Giordano and B. S. Yeo, *J. Mater. Chem. A*, 2015, **3**, 8361–8368.
8 M. Zhou, Q. Weng, Z. I. Popov, Y. Yang, L. Y. Antipina, P. B. Sorokin, X. Wang, Y. Bando and D. Golberg, *ACS Nano*, 2018, **12**, 4148–4155.
9 B. Liu, B. He, H. Q. Peng, Y. Zhao, J. Cheng, J. Xia, J. Shen, T. W. Ng, X. Meng, C. S. Lee and W. Zhang, *Adv. Sci.*, 2018, **5**, 1800406.
10 G. Chen, T. Ma, Z. Liu, N. Li, Y. Su, K. Davey and S. Qiao, *Adv. Funct. Mater.*, 2016, **26**, 3314–3323.
11 Y. Shi and B. Zhang, *Chem. Soc. Rev.*, 2016, **45**, 1529–1541.
12 J. Kibsgaard, Z. Chen, B. N. Reinecke and T. F. Jaramillo, *Nat. Mater.*, 2012, **11**, 963–969.
13 P. D. Tran, T. V. Tran, M. Orio, S. Torelli, Q. D. Truong, K. Nayuki, Y. Sasaki, S. Y. Chiam, R. Yi, I. Honma, J. Barber and V. Artero, *Nat. Mater.*, 2016, **15**, 640–646.
14 D. S. Kong, J. J. Cha, H. T. Wang, H. R. Lee and Y. Cui, *Energy Environ. Sci.*, 2013, **6**, 3553–3558.
15 A. Sivanantham, P. Ganesan and S. Shanmugam, *Adv. Funct. Mater.*, 2016, **26**, 4661–4672.
16 Z. Peng, D. S. Jia, A. M. Al-Enizi, A. A. Elzatahry and G. F. Zheng, *Adv. Energy Mater.*, 2015, **5**, 1402031.
17 J. Deng, H. Li, S. Wang, D. Ding, M. Chen, C. Liu, Z. Tian, K. S. Novoselov, C. Ma, D. Deng and X. Bao, *Nat. Commun.*, 2017, **8**, 14430.
18 J. Xie, J. Zhang, S. Li, F. Grote, X. Zhang, H. Zhang, R. Wang, Y. Lei, B. Pan and Y. Xie, *J. Am. Chem. Soc.*, 2013, **135**, 17881–17888.
19 T. Kou, T. Smart, B. Yao, I. Chen, D. Thota, Y. Ping and Y. Li, *Adv. Energy Mater.*, 2018, **8**, 1703538.
20 J. Zhou, G. Fang, A. Pan and S. Liang, *ACS Appl. Mater. Interfaces*, 2016, **8**, 33681–33689.
21 J. Huang, D. Hou, Y. Zhou, W. Zhou, G. Li, Z. Tang, L. Li and S. Chen, *J. Mater. Chem. A*, 2015, **3**, 22886–22891.
22 Y. Yang, K. Zhang, H. Ling, X. Li, H. Chan, L. Yang and Q. Gao, *ACS Catal.*, 2017, **7**, 2357–2366.
23 J. Zhang, T. Wang, D. Pohl, B. Rellinghaus, R. Dong, S. Liu, X. Zhuang and X. Feng, *Angew. Chem., Int. Ed.*, 2016, **55**, 6702–6707.
24 N. K. Chaudhari, H. Jin, B. Kim and K. Lee, *Nanoscale*, 2017, **9**, 12231–12247.
25 X. Q. Du, Q. B. Wang and X. S. Zhang, *New J. Chem.*, 2018, **42**, 18201–18207.
26 Q. Ma, C. Hu, K. Liu, S. Hung, D. Ou, H. Chen, G. Fu and N. Zheng, *Nano Energy*, 2017, **41**, 148–153.
27 W. Xiao, J. S. Chen, C. M. Li, R. Xu and X. W. Lou, *Chem. Mater.*, 2010, **22**, 746–754.
28 Z. X. Yin, Y. J. Chen, Y. Zhao, C. Y. Li, C. L. Zhu and X. T. Zhang, *J. Mater. Chem. A*, 2015, **3**, 22750–22758.
29 D. Cai, B. Liu, D. Wang, L. Wang, Y. Liu, H. Li, Y. Wang, Q. Li and T. Wang, *J. Mater. Chem. A*, 2014, **2**, 4954–4960.
30 L. Q. Mai, F. Yang, Y. L. Zhao, X. Xu, L. Xu and Y. Z. Luo, *Nat. Commun.*, 2011, **2**, 381.
31 L. Zhang, S. Zheng, L. Wang, H. Tang, H. Xue, G. Wang and H. Pang, *Small*, 2017, **13**, 1700917.
32 S. J. Peng, L. L. Li, H. B. Wu, S. Madhavi and X. W. Lou, *Adv. Energy Mater.*, 2015, **5**, 1401172.
33 Z. Yin, S. Zhang, Y. Chen, P. Gao, C. Zhu, P. Yang and L. Qi, *J. Mater. Chem. A*, 2015, **3**, 739–745.
34 J. Wang, X. Zhang, Q. Wei, H. Lv, Y. Tian, Z. Tong, X. Liu, J. Hao, H. Qu, J. Zhao, Y. Li and L. Mai, *Nano Energy*, 2016, **19**, 222–233.
35 T. C. An, Y. Wang, J. Tang, W. Wei, X. Q. Cui, A. M. Alenizi, L. J. Zhang and G. F. Zheng, *J. Mater. Chem. A*, 2016, **4**, 13439–13443.
36 D. Guo, H. Zhang, X. Yu, M. Zhang, P. Zhang, Q. Li and T. Wang, *J. Mater. Chem. A*, 2013, **1**, 7247–7254.
37 J. Wang, S. K. Liu, X. Zhang, X. S. Liu, X. X. Liu, N. Li, J. P. Zhao and Y. Li, *Electrochim. Acta*, 2016, **213**, 663–671.
38 I. Hussain, A. Ali, C. Lamiel, S. G. Mohamed, S. Sahoo and J. J. Shim, *Dalton Trans.*, 2019, **48**, 3853–3861.
39 F. Wang, J. Zhao, W. Tian, Z. Hu, X. Lv, H. Zhang, H. Yue, Y. Zhang, J. Ji and W. Jiang, *RSC Adv.*, 2019, **9**, 1562–1569.
40 L. Huang, J. W. Xiang, W. Zhang, C. J. Chen, H. H. Xu and Y. H. Huang, *J. Mater. Chem. A*, 2015, **3**, 22081–22087.
41 H. Vrubel, D. Merki and X. Hu, *Energy Environ. Sci.*, 2012, **5**, 6136–6144.
42 J. Jiang, M. Gao, W. Sheng and Y. Yan, *Angew. Chem., Int. Ed.*, 2016, **55**, 15240–15245.
43 H. Zhu, J. Zhang, R. Yanzhang, M. Du, Q. Wang, G. Gao, J. Wu, G. Wu, M. Zhang, B. Liu, J. Yao and X. Zhang, *Adv. Mater.*, 2015, **27**, 4752–4759.
44 Z. Ma, H. Meng, M. Wang, B. Tang, J. Li and X. Wang, *ChemElectroChem*, 2018, **5**, 335–342.
45 F. Z. Wang, M. J. Zheng, B. Zhang, C. Q. Zhu, Q. Li, L. Ma and W. Z. Shen, *Sci. Rep.*, 2016, **6**, 31092.
46 L. L. Feng, G. Yu, Y. Wu, G. D. Li, H. Li, Y. Sun, T. Asefa, W. Chen and X. Zou, *J. Am. Chem. Soc.*, 2015, **137**, 14023–14026.
47 X. Han, X. Wu, Y. Deng, J. Liu, J. Lu, C. Zhong and W. Hu, *Adv. Energy Mater.*, 2018, **8**, 1800935.
48 R. Miao, B. Dutta, S. Sahoo, J. He, W. Zhong, S. A. Cetegen, T. Jiang, S. P. Alpay and S. L. Suib, *J. Am. Chem. Soc.*, 2017, **139**, 13604–13607.
49 C. Ouyang, X. Wang, C. Wang, X. Zhang, J. Wu, Z. Ma, S. Dou and S. Wang, *Electrochim. Acta*, 2015, **174**, 297–301.
50 N. H. Attanayake, A. C. Thenuwara, A. Patra, Y. V. Aulin, T. M. Tran, H. Chakraborty, E. Borguet, M. L. Klein, J. P. Perdew and D. R. Strongin, *ACS Energy Lett.*, 2018, **3**, 7–13.
51 Y. Yin, Y. Zhang, T. Gao, T. Yao, X. Zhang, J. Han, X. Wang, Z. Zhang, P. Xu, P. Zhang, X. Cao, B. Song and S. Jin, *Adv. Mater.*, 2017, **29**, 1700311.

52 J. Deng, H. Li, J. Xiao, Y. Tu, D. Deng, H. Yang, H. Tian, J. Li, P. Ren and X. Bao, *Energy Environ. Sci.*, 2015, **8**, 1594–1601.
53 J. Li, J. Kang, Q. Cai, W. Hong, C. Jian, W. Liu and K. Banerjee, *Adv. Mater. Interfaces*, 2017, **4**, 1700303.
54 Y. Cheng, S. K. Lu, F. Liao, L. Liu, Y. Li and M. Shao, *Adv. Funct. Mater.*, 2017, **27**, 1700359.
55 L. L. Chen, W. X. Yang, X. J. Liu and J. B. Jia, *Int. J. Hydrogen Energy*, 2017, **42**, 12246–12253.
56 W. Xin, W. J. Jiang, Y. Lian, H. Li, S. Hong, S. Xu, H. Yan and J. S. Hu, *Chem. Commun.*, 2019, **55**, 3781–3784.
57 H. Zhu, G. Gao, M. Du, J. Zhou, K. Wang, W. Wu, X. Chen, Y. Li, P. Ma, W. Dong, F. Duan, M. Chen, G. Wu, J. Wu, H. Yang and S. Guo, *Adv. Mater.*, 2018, **30**, 1707301.
58 C. Wang, B. Tian, M. Wu and J. Wang, *ACS Appl. Mater. Interfaces*, 2017, **9**, 7084–7090.
59 Y. Guo, L. Gan, C. Shang, E. Wang and J. Wang, *Adv. Funct. Mater.*, 2017, **27**, 1602699.
60 J. Hou, B. Zhang, Z. Li, S. Cao, Y. Sun, Y. Wu, Z. Gao and L. Sun, *ACS Catal.*, 2018, **8**, 4612–4621.
61 N. Huang, Y. Ding, S. Yan, L. Yang, P. Sun, C. Huang and X. Sun, *ACS Appl. Energy Mater.*, 2019, **2**, 6751–6760.
62 Y. Zhu, L. F. Song, N. Song, M. X. Li, C. Wang and X. F. Lu, *ACS Sustainable Chem. Eng.*, 2019, **7**, 2899–2905.
63 G. Solomon, R. Mazzaro, S. You, M. M. Natile, V. Morandi, I. Concina and A. Vomiero, *ACS Appl. Mater. Interfaces*, 2019, **11**, 22380–22389.
64 V. Vij, S. Sultan, A. M. Harzandi, A. Meena, J. N. Tiwari, W. G. Lee, T. Yoon and K. S. Kim, *ACS Catal.*, 2017, **7**, 7196–7225.
65 J. H. Wang, W. Cui, Q. Liu, Z. C. Xing, A. M. Asiri and X. P. Sun, *Adv. Mater.*, 2016, **28**, 215–230.
66 X. Wang, Y. Zhang, H. Si, Q. Zhang, J. Wu, L. Gao, X. Wei, Y. Sun, Q. Liao, Z. Zhang, K. Ammarah, L. Gu, Z. Kang and Y. Zhang, *J. Am. Chem. Soc.*, 2020, DOI: 10.1021/jacs.9b12113.
67 J. Zhang, T. Wang, P. Liu, S. Liu, R. Dong, X. Zhuang, M. Chen and X. Feng, *Energy Environ. Sci.*, 2016, **9**, 2789–2793.
68 B. S. Tang, Z. G. Yu, Y. X. Zhang, C. H. Tang, H. L. Seng, Z. W. Seh, Y. W. Zhang, S. J. Pennycook, H. Gong and W. F. Yang, *J. Mater. Chem. A*, 2019, **7**, 13339–13346.